

# SIGNATURES OF FOREGROUND SKY IN POWER SPECTRA OF REDSHIFTED NEUTRAL HYDROGEN FROM THE EPOCH OF REIONIZATION

NITHYANANDAN THYAGARAJAN<sup>1</sup>, DANIEL C. JACOBS<sup>1</sup>, JUDD D. BOWMAN<sup>1</sup>, A. P. BEARDSLEY<sup>2</sup>, B. J. HAZELTON<sup>2</sup>, M. F. MORALES<sup>2</sup>, J. POBER<sup>2</sup>, I. S. SULLIVAN<sup>2</sup>, T. PRABU<sup>3</sup>, G. BERNARDI<sup>4</sup>, F. BRIGGS<sup>5</sup>, R. J. CAPPALLO<sup>6</sup>, B. E. COREY<sup>6</sup>, A. A. DESHPANDE<sup>3</sup>, D. EMRICH<sup>7</sup>, B. M. GAENSLER<sup>8,9</sup>, R. GOEKE<sup>10</sup>, L. J. GREENHILL<sup>11</sup>, M. JOHNSTON-HOLLITT<sup>12</sup>, D. L. KAPLAN<sup>13</sup>, J. C. KASPER<sup>14,11</sup>, E. KRATZENBERG<sup>6</sup>, C. J. LONSDALE<sup>6</sup>, M. J. LYNCH<sup>7</sup>, S. R. MCWHIRTER<sup>6</sup>, D. A. MITCHELL<sup>15,9</sup>, E. MORGAN<sup>10</sup>, D. OBEROI<sup>16</sup>, S. M. ORD<sup>7,9</sup>, A. E. E. ROGERS<sup>6</sup>, A. ROSHI<sup>17</sup>, N. UDAYA SHANKAR<sup>3</sup>, K. S. SRIVANI<sup>3</sup>, R. SUBRAHMANYAN<sup>3,9</sup>, S. J. TINGAY<sup>7,9</sup>, M. WATERSON<sup>7,5</sup>, R. B. WAYTH<sup>7,9</sup>, R. L. WEBSTER<sup>18,9</sup>, A. R. WHITNEY<sup>6</sup>, A. WILLIAMS<sup>7</sup>, C. L. WILLIAMS<sup>10</sup>

*Draft version September 3, 2014*

## ABSTRACT

We characterize signatures of foreground radio emission and instrument configuration on the observed power spectra of redshifted HI 21 cm line emission from the epoch of reionization (EoR) using an antenna pair based “delay spectrum” analysis technique. We use the 128-tile Murchison Widefield Array (MWA) instrument configuration for our studies. We simulate the delay spectrum response of interferometers, for the first time, to an all-sky foreground model consisting of diffuse and compact Galactic and extragalactic emission. By tying model parameters to those of a subset of first season of observing with the MWA, our simulations agree with the observed data to within expected uncertainty. A wedge-shaped region of foreground contamination and a spillover from this contamination into relatively foreground-free regions (*EoR window*) in the delay spectrum due to spectral properties of foreground emission and the instrument is confirmed. Due to shortening of antenna spacings caused by projection effects, diffuse emission produces edge-heavy *two-pronged fork*-like features even on wide antenna spacings, hitherto not predicted. Features in the inner regions of the wedge are predominantly due to compact foreground objects. This results in a *pitchfork*-shaped delay spectrum. The bright Galactic center severely contaminates the *EoR window* on certain antenna spacings in certain observations. For such cases, we present an effective practical tool for screening interferometers with high foreground contamination and mitigating their effects on EoR data analysis.

**Keywords:** large-scale structure of Universe — methods: statistical — radio continuum: galaxies — radio lines: general — reionization — techniques: interferometric

<sup>1</sup> School of Earth and Space Exploration, Arizona State University, Tempe, AZ 85287, USA; e-mail: t.nithyanandan@asu.edu

<sup>2</sup> Department of Physics, University of Washington, Seattle, WA 98195, USA

<sup>3</sup> Raman Research Institute, Bangalore 560080, India

<sup>4</sup> Square Kilometre Array South Africa (SKA SA), Cape Town 7405, South Africa

<sup>5</sup> Research School of Astronomy and Astrophysics, Australian National University, Canberra, ACT 2611, Australia

<sup>6</sup> MIT Haystack Observatory, Westford, MA 01886, USA

<sup>7</sup> International Centre for Radio Astronomy Research, Curtin University, Bentley, WA 6102, Australia

<sup>8</sup> Sydney Institute for Astronomy, School of Physics, The University of Sydney, NSW 2006, Australia

<sup>9</sup> ARC Centre of Excellence for All-sky Astrophysics (CAASTRO)

<sup>10</sup> Kavli Institute for Astrophysics and Space Research, Massachusetts Institute of Technology, Cambridge, MA 02139, USA

<sup>11</sup> Harvard-Smithsonian Center for Astrophysics, Cambridge, MA 02138, USA

<sup>12</sup> School of Chemical & Physical Sciences, Victoria University of Wellington, Wellington 6140, New Zealand

<sup>13</sup> Department of Physics, University of Wisconsin–Milwaukee, Milwaukee, WI 53201, USA

<sup>14</sup> Department of Atmospheric, Oceanic and Space Sciences, University of Michigan, Ann Arbor, MI 48109, USA

<sup>15</sup> CSIRO Astronomy and Space Science (CASS), PO Box 76, Epping, NSW 1710, Australia

<sup>16</sup> National Centre for Radio Astrophysics, Tata Institute for Fundamental Research, Pune 411007, India

<sup>17</sup> National Radio Astronomy Observatory, Charlottesville and Greenbank, USA

<sup>18</sup> School of Physics, The University of Melbourne, Parkville, VIC 3010, Australia

## 1. INTRODUCTION

After the CMB epoch, the period in the history of the universe often referred to as the *dark ages*, followed the epoch of reionization (EoR). This was a period of non-linear growth of density perturbations and astrophysical evolution. Studying the epoch of reionization holds the key to understanding this evolution. Recently, observing the redshifted 21 cm spin transition of neutral hydrogen has emerged as a very promising experiment to fill the gaps in our understanding of the universe's history.

Sensitive instruments such as the Square Kilometer Array (SKA) are required for direct observation and tomography of redshifted HI. Numerous precursors to the SKA such as the Murchison Widefield Array (MWA; Lonsdale et al. 2009; Tingay et al. 2013), the Low Frequency Array (LOFAR; van Haarlem et al. 2013), and the Precision Array for Probing the Epoch of Reionization (PAPER; Parsons et al. 2010) have become operational with enough sensitivity for a statistical detection of the EoR HI power spectrum.

One of the key challenges in the statistical detection of power spectrum of the redshifted HI signal arises from the contamination by Galactic and extragalactic foregrounds (see, e.g., Di Matteo et al. 2002; Zaldarriaga et al. 2004; Furlanetto et al. 2006). Morales & Hewitt (2004) show that the inherent isotropy and symmetry of the EoR signal in frequency and spatial wavenumber ( $k$ ) space make it distinguishable from sources of contamination which lack such symmetry. Foreground removal techniques rely on the spectral smoothness of foreground emission (Morales et al. 2006; Bowman et al. 2009; Liu & Tegmark 2011; Parsons et al. 2012; Dillon et al. 2013).

Precise understanding of these foreground signatures is necessary in order to remove foreground systematics from the measured power spectrum. Considerable effort has been made in mapping the residual foreground signatures in observed power spectrum (Thyagarajan et al. 2013; Poher et al. 2013; Morales et al. 2012; Trott et al. 2012; Datta et al. 2010; Bowman et al. 2009) after foreground subtraction.

In this paper, in one of the most detailed characterizations to date, using an interferometer (antenna pair) based delay spectrum technique, we demonstrate the signatures of unsubtracted diffuse and compact foreground models in delay spectrum, a quantity closely related to the sought power spectrum. The simplicity of this technique and usage of basic interferometric visibility data Fourier transformed along frequency (delay spectrum) on individual interferometers offer very effective diagnostics for scheduling observations and data analysis, and an insightful view onto foreground signatures in the EoR HI power spectrum. We explore the diversity in these signatures as a function of observation and instrument parameters and confirm our findings with data obtained from the MWA. This simple technique allows us to predict foreground signatures, hitherto not predicted.

We have organized this paper as follows. §2 defines the delay spectrum and its relation to the power spectrum. §3 and §4 describe the MWA instrumental parameters and observation parameters used in this study respectively. Analysis of data obtained with the MWA is described in §5. In §6, we describe the building blocks of our delay spectrum modeling including the models used

for the antenna power pattern and foreground. Here, we also establish that the results of modeling and data analysis agree with each other. In §7, we present a detailed analysis of the signatures of foregrounds on the modeled delay spectrum and its dependence on instrumental and observation parameters. In §8, we use our understanding to grade interferometers based on the amount of foreground contamination estimated by the delay spectrum technique. In §9, we present our summary and conclusions.

## 2. DELAY SPECTRUM

Interferometer array data known as *visibilities*,  $V_f(\bar{\mathbf{u}}, f)$ , represent correlations between time-series of electric fields measured by different antenna pairs with separation vectors  $\bar{\mathbf{x}}$  and then Fourier transformed along time axis to obtain a spectrum along frequency ( $f$ ) axis. Here,  $\bar{\mathbf{u}} \equiv \bar{\mathbf{x}}f/c \equiv \bar{\mathbf{x}}/\lambda$ ,  $c$  is the speed of light and  $\lambda$  is the wavelength.  $\bar{\mathbf{u}}$  is related to transverse spatial frequency modes ( $\bar{\mathbf{k}}_\perp$ ) of brightness distribution of the sky as  $\bar{\mathbf{k}}_\perp \equiv 2\pi\bar{\mathbf{u}}/D(z)$ , where  $D(z)$  is the transverse comoving distance at a redshift  $z$ . If  $I(\bar{\mathbf{l}}, f)$  is the emission at different frequencies on the sky as a function of direction unit vector ( $\bar{\mathbf{l}}$ ) specified as direction cosines,  $V_f(\bar{\mathbf{u}}, f)$  represents the Fourier decomposition of  $I(\bar{\mathbf{l}}, f)$  attenuated by the antenna's angular power pattern  $A(\bar{\mathbf{l}}, f)$ , into transverse spatial frequency modes. Taking into account the instrumental bandpass weights  $W_f(f)$ , this relation can be written as:

$$V_f(\bar{\mathbf{u}}, f) = \int A(\bar{\mathbf{l}}, f) I(\bar{\mathbf{l}}, f) W_f(f) e^{-i2\pi\bar{\mathbf{u}}\cdot\bar{\mathbf{l}}} d^2\bar{\mathbf{l}}. \quad (1)$$

We define the *delay spectrum*  $V_\eta(\bar{\mathbf{u}}, \eta)$  to be the inverse Fourier transform of  $V_f(\bar{\mathbf{u}}, f)$  along the frequency coordinate:

$$V_\eta(\bar{\mathbf{u}}, \eta) = \int V_f(\bar{\mathbf{u}}, f) W'_f(f) e^{i2\pi\eta f} df, \quad (2)$$

where,  $W'_f(f)$  is a frequency window weighting function which can be chosen to control the quality of the delay spectrum (Thyagarajan et al. 2013; Vedantham et al. 2012).  $\eta$  represents the signal delay between the antenna pairs in an interferometer given by:

$$\eta = \frac{\bar{\mathbf{x}} \cdot \bar{\mathbf{l}}}{c} = \frac{\bar{\mathbf{u}} \cdot \bar{\mathbf{l}}}{f}. \quad (3)$$

The terms delay and lag are used interchangeably in this paper.

Since we are studying a redshifted HI spectral line,  $f$  is a measure of cosmological distance along the line of sight. Consequently,  $\eta$  is a measure of line of sight spatial frequency mode,  $k_\parallel$ . Thus,  $|V_\eta(\bar{\mathbf{u}}, \eta)|^2$  is directly related to the spatial power spectrum of redshifted HI distribution,  $|V(\bar{\mathbf{k}}_\perp, k_\parallel)|^2$ . However, foreground objects emit in radio frequencies and contaminate the signals from the redshifted HI. Due to their spatial and spectral properties,  $V_\eta(\bar{\mathbf{u}}, \eta)$  also contains contamination from foreground radio sources (Thyagarajan et al. 2013; Trott et al. 2012; Morales et al. 2012; Bowman et al. 2009). These contaminations have to be characterized precisely in order to reduce their impact on redshifted HI power spectrum detection sensitivity.

In summary,  $V_\eta(\bar{\mathbf{u}}, \eta)$ , is closely related to visibilities,  $V_f(\bar{\mathbf{u}}, f)$ , the basic data blocks measured by an interferometer, as seen from equation 2. It captures all the effects of EoR HI signal corruption caused by foregrounds and the instrument. At the same time, it is very closely related to the sought power  $|V(\bar{\mathbf{k}}_\perp, k_\parallel)|^2$  in  $k$ -modes containing critical information about spatial scales. For our analysis, we use an equivalent quantity,  $V_\eta(\bar{\mathbf{x}}, \eta) \equiv V_\eta(\lambda \bar{\mathbf{u}}, \eta)$ . For purposes of illustration, we often use a simplified quantity  $|V_\eta(|\bar{\mathbf{x}}|, \eta)|$ .

We now describe in detail an important ingredient, the MWA instrument.

### 3. INSTRUMENT PARAMETERS

We use the 128-tile layout of the MWA (Beardsley et al. 2012) and choose a center frequency of 185 MHz with a bandwidth of 30.72 MHz divided into 384 frequency channels each of width 80 kHz. The choice of center frequency translates to  $z \approx 6.68$  for the 21 cm spin flip transition of H I. The bandwidth was chosen to be close to the maximum instantaneous value of the MWA in order to maximize the resolution in delay coordinates and obtain detailed characteristics of delay spectra from foregrounds. We restrict our analysis to the innermost antenna spacings with  $|\bar{\mathbf{x}}| \leq x_{\max} = 200$  m, or  $|\bar{\mathbf{u}}| \leq u_{\max} = 123$  at a frequency of 185 MHz. These interferometers are responsive to transverse spatial structures on scales  $\gtrsim 1/u_{\max} \approx 28'$ . Hereafter, we use the terms tile and antenna interchangeably to refer to the MWA tile.

The bandpass weights in the frequency window of the MWA are obtained through a 8-tap Polyphase Filter Bank (PFB) using a Kaiser window with the  $\beta$  parameter set to 5. The bandpass weights consist of coarse frequency channels of width 1.28 MHz each of which contains 16 finer frequency channels of width 80 kHz. Our analysis, therefore, contains 24 coarse channels. As the data are subsequently bandpass calibrated, the bandpass weights are normalized to unity. But the edges of the coarse channels are noisy and aliased from adjacent coarse channels. Thus, we remove one fine channel from each side of the coarse channel edges from our data. This constitutes  $W_f(f)$  in equation 1. The bandpass properties used in this paper are illustrated in figure 1.

Thermal noise in simulated visibilities is estimated assuming a system temperature of  $T_{\text{sys}} = 90$  K per polarization for all frequency channels for all interferometers throughout the course of observation. We take into account the increase in thermal uncertainty in frequency channels that results due to aforementioned bandpass correction.

### 4. OBSERVATION PARAMETERS

One of the primary targets for EoR observing with the MWA is a patch of sky centered around RA = 00h 00m 00.00s, Dec =  $-30^\circ 00' 00''$ . This is one of the regions of low foreground emission within  $27^\circ$  from the zenith. The MWA tracks a patch of sky through antenna beams formed and steered electronically by controlling delay settings of an array of dipoles in a MWA tile. These beamformer delay settings can be changed only in discrete steps. Accordingly, observations were made in a “drift and shift” (D-S) mode. Figure 2 shows the direction of pointing of MWA tiles during the course of the

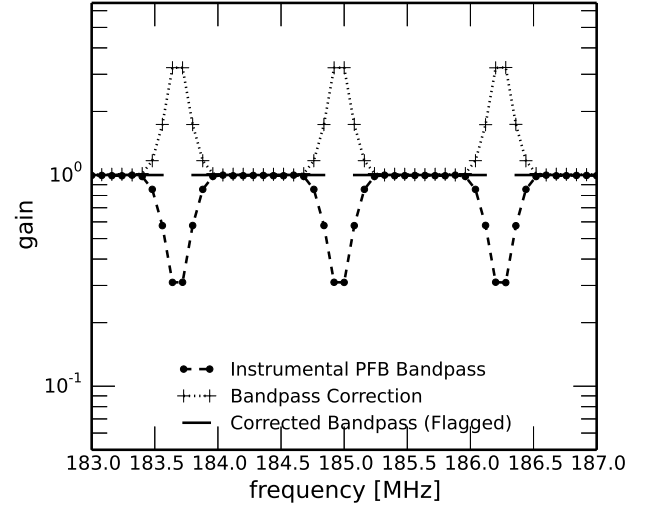


**Figure 1.** Bandpass properties used in modeling and analysis of delay spectrum of MWA visibilities. The filled circles joined by dotted lines show the 8-tap PFB bandpass shapes obtained using a Kaiser window with parameter  $\beta = 5$ . The plus symbols joined by dashed lines are the bandpass correction factors. The solid line shows the flagged (gaps) and gain-corrected bandpass shape,  $W_f(f)$ . These shapes are repeated every 1.28 MHz for the entire bandwidth of 30.72 MHz centered around 185 MHz.

observation. The sky is allowed to drift for a certain period of time (usually  $\sim 30$  mins) before the discrete shifts in the beamformer delay settings position the beam to be centered again on the same patch of sky. This process is repeated throughout the course of the observation  $\approx 4.86$  hours. The LST of two snapshots we chose for our study are shown as vertical lines at -1.92 hours (wrapped by  $360^\circ$  from 22.08 hours) and 0.09 hours which are hereafter denoted as *off-zenith* and *zenith* pointings respectively. These pointings (phased array power patterns) are centered at RA =  $4^{\text{h}}38^{\text{m}}7^{\text{s}}$ , Dec =  $-29^\circ 8'$  and RA =  $-28^\circ 8'$ , Dec =  $-26^\circ 7'01''$ , whereas the visibilities themselves are phased to zenith corresponding to RA =  $-28^\circ 8'$ , Dec =  $-26^\circ 7'01''$ , and RA =  $1^{\text{h}}35^{\text{m}}$ , Dec =  $-26^\circ 7'01''$  respectively.

Throughout this paper,  $\bar{\mathbf{u}}$  and  $\bar{\mathbf{x}}$  are assumed to be on a coordinate system aligned with the local east, north (along local meridian) and upward directions at the MWA site. For the conventions of Fourier transform and its inverse we use in this paper, in accordance with equation 3, signals from the sky towards east and north are recorded with positive delays on eastward and northward oriented antenna spacings respectively. For instance, at the beginning of the observation, the Galactic center is in the westward sky just about to set. Signals from this direction are recorded with a negative delay on interferometers whose antenna spacings are oriented towards the east. Similarly, signals from directions eastward of the local meridian arrive with positive delays on eastward oriented antenna spacings.

For geometrical intuition, we restrict the orientation ( $\theta_b$ , measured anti-clockwise from East) of all antenna spacings to lie in the range  $-67.5^\circ \leq \theta_b < 112.5^\circ$ . Interferometers with antenna spacings oriented in the other half-plane measure conjugate visibilities with delays of equal magnitude but of opposite sign and hence are ignored in our analysis.

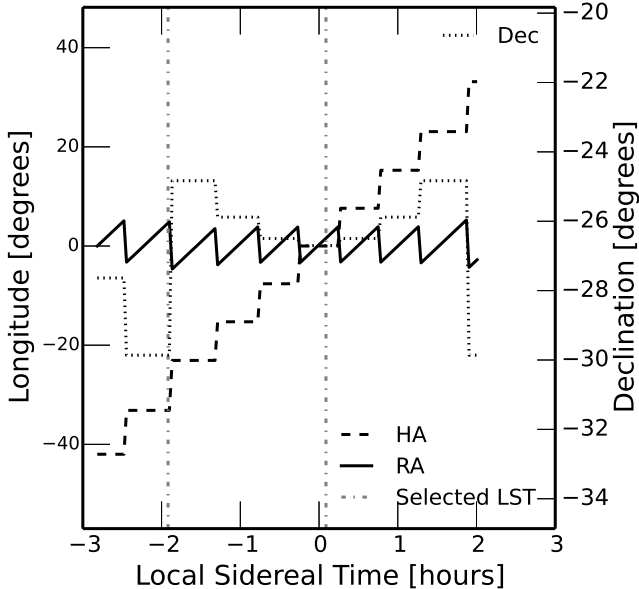


**Figure 2.** MWA tile beam pointing directions during the course of the observation. The x-axis refers to the Local Sidereal Time (LST) in hours. The axis on the left refers to longitudes, namely, Right Ascension (RA) and Hour Angle (HA) in degrees. Negative values of RA, HA, and LST are to be interpreted as having been wrapped around by  $360^\circ$  or 24 hours. The axis on the right refers to the declination of the pointing direction. The RA, HA, and declination are plotted with solid, dashed and dotted line styles respectively. A “drift and shift” scheme is used. The sky is allowed to drift for  $\sim 30$  mins before the beamformer delay settings change in a discrete step to center the beam around RA = 00h 00m 00.00s, Dec =  $-30^\circ 00' 00''$ . Dot-dashed vertical lines show the LST of off-zenith and zenith pointings used in our study.

## 5. DATA ANALYSIS

### 5.1. Imaging and deconvolution

Describe the FHD data analysis up to the point of getting calibrated visibilities here.

### 5.2. Deconvolution along Delay Axis

We obtain the delay spectrum of these calibrated visibilities using equation 2 while choosing  $W_f'(f)$  to be a *Blackman–Harris* window function. Due to periodic gaps in frequency bandpass occurring in intervals of 1.28 MHz (see figure 1), the delay spectrum is expected to contain harmonics of actual foreground emission repeated at intervals of  $0.78 \mu\text{s}$ . Hence, we have employed deconvolution by *CLEAN* algorithm (Taylor et al. 1999) along the delay axis (Parsons & Backer 2009; Parsons et al. 2012) to rid the delay spectra of such artifacts. The convolving kernel for the algorithm is given by the inverse Fourier transform of the instrumental bandpass shape.

### 5.3. Delay Spectrum after Delay Deconvolution

We show results of delay spectrum from MWA data after deconvolution along delay axis in figure 3. Boundaries of the *foreground wedge* are also shown. The *off-zenith* pointing has emission notably higher than in the *zenith* pointing inside the wedge boundaries. This is shown later to be due to response of the interferometer array to the bright Galactic center and Galactic plane in the westward sky. Consequently, the contamination into the *EoR win-*

dow is also higher. Emission in *zenith* pointing is more centrally concentrated due to phasing of power pattern to the zenith, whereas the *off-zenith* pointing has a power pattern phased eastward of zenith and is also responsive to emission from angles far away from zenith.

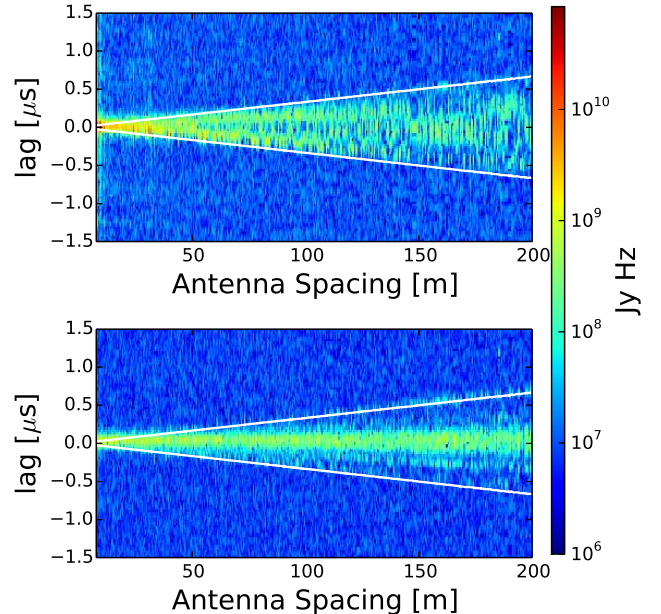


**Figure 3.** Delay spectrum amplitude,  $|V_\eta(|\vec{x}|, \eta)|$  (in units of Jy Hz), obtained with MWA data for *off-zenith* (top) and *zenith* (bottom) pointings. White lines mark the boundaries of *foreground wedge* determined by the horizon delay limit and antenna spacing. The features in the wedge appear to be brighter and the spillover contamination appears to be higher in the *off-zenith* pointing relative to the *zenith* pointing due to the presence of brighter foregrounds such as the Galactic center and the Galactic plane. The logarithmic color scale (shown at the right) is common to both panels.

Despite delay deconvolution, we still see leakage beyond the cleaned regions indicating the inability of the deconvolution algorithm to fit the data perfectly. This is predominant at short antenna spacings. This is because the maximum delay envelope (boundary of the wedge) consists of mixed emission from large portions of the sky into a narrow range of delays and the deconvolution algorithm does not have sufficient support in delay space to fit the delay spectrum. However, we wish to emphasize that the purpose of deconvolution is to rid the delay spectra of instrumental artifacts to the best extent possible in order to see the underlying signatures of foreground emission. It is not our intention in this paper to use the deconvolution as a foreground removal tool. Hence, our discussion and conclusions are valid despite imperfections in deconvolution.

## 6. DELAY SPECTRUM MODELING

We describe power pattern and foreground models we have used in modeling the measured delay spectra.

### 6.1. Power pattern

The power pattern of a MWA tile,  $A(\vec{l}, f)$  in equation 1, over the entire hemisphere is analytically modeled based on a  $4 \times 4$  phased array of isotropic radiators at a height

of 0.3 m above an infinite ground plane. We also assume that the delay corrections during the phased addition of dipole voltages in the beamformer suffer from random fluctuations of rms 0.05 ns. The models of power pattern used in data analysis take into account effects of mutual coupling of dipoles in the tile besides finite ground plane effects. Our models were found to be in reasonable agreement with those used in the data analysis.

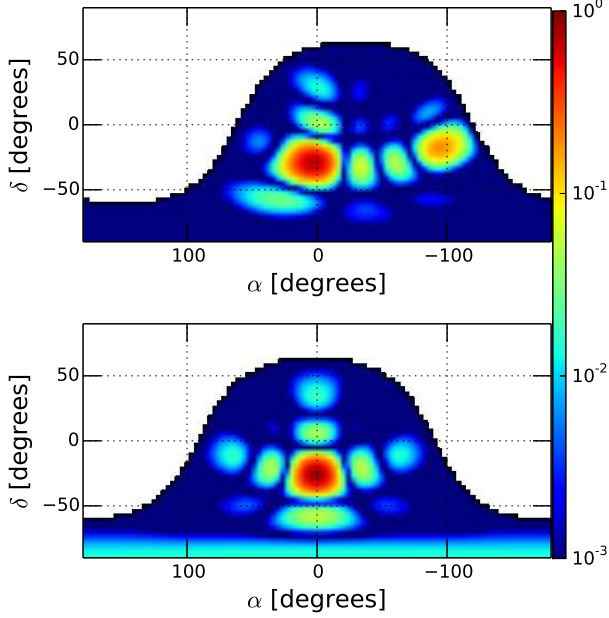


**Figure 4.** Models of MWA tile power pattern in Right Ascension ( $\alpha$ ) and Declination ( $\delta$ ) coordinates for the off-zenith (top) and zenith pointings (bottom) at 185 MHz. An MWA tile is modeled as a  $4 \times 4$  array of isotropic radiators placed 0.3 m above the ground plane. Random fluctuations of rms 0.05 ns have been added to delay corrections during the phased addition of voltages from these isotropic radiators. The logarithmic color scale (shown at the right) is common to both panels.

### 6.2. Foreground Model

An instrument such as the MWA has a very wide field of view ( $\gtrsim 20^\circ$  at 185 MHz) for imaging purposes. In the context of EoR HI power spectrum, it has been known that unsubtracted foreground sources anywhere in the visible hemisphere up to the horizon directly contaminate the spatial frequency modes in the power spectrum. In addition, this contamination also spills over into the relatively cleaner regions, called *EoR window*, due to spectral properties of the instrument and the foregrounds (Thyagarajan et al. 2013; Pober et al. 2013; Vedantham et al. 2012; Parsons et al. 2012). Thus, it is important to consider an all-sky model for foreground objects in evaluating the features seen in the power spectrum instead of restricting to the primary field of view.

Beardsley et al. (2013) estimated the sensitivity of the MWA to EoR HI power spectrum detection taking into account thermal noise effects in the *EoR window*. Thyagarajan et al. (2013) estimated the sensitivity taking into account the spillover from foreground contamination from unsubtracted extragalactic point sources in the *EoR window* besides thermal noise. In this paper, we include

the diffuse Galactic emission for enhancing our understanding of foreground signatures in the power spectrum. We use an all-sky foreground emission model that consists of diffuse and bright compact components.

#### 6.2.1. Diffuse Foreground Model

For the diffuse component, we use an all-sky radio foreground model (de Oliveira-Costa et al. 2008) to estimate the emission at 185 MHz. Since this map is predominantly based on the 408 MHz all-sky map of Haslam et al. (1982) which has an angular resolution of  $0.85'$ , we smoothed the 185 MHz diffuse emission map to the same resolution. However, to avoid any artifacts from sampling this map, we sample it at  $\approx 27'$  intervals. Using the same source model, we also obtain the diffuse emission maps at 170 MHz and 200 MHz to estimate the spectral index map of the diffuse emission model.

A low resolution version of the diffuse foreground model used is shown in figure 5. Contours of the MWA tile power pattern shown in figure 4 are also overlaid. Of notable significance in the *off-zenith* pointing is the presence of a portion of the Galactic plane and the bright Galactic center in the visible hemisphere in the westward sky and the MWA tile's power receptivity is significantly high ( $\gtrsim 0.125$ ) in that direction. In the *zenith* pointing, the Galactic plane has almost set and the contour level of power pattern in that direction is at least 16 times lesser.

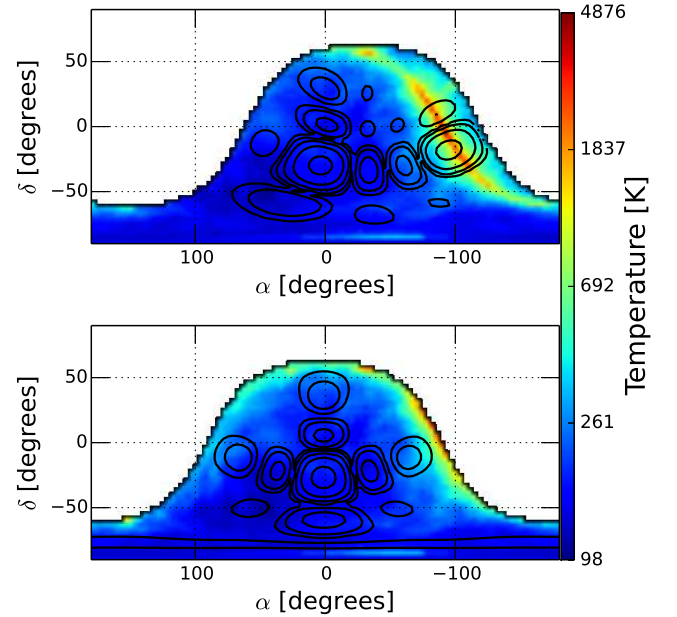


**Figure 5.** Sky brightness temperature (in K) of the diffuse foreground model at 185 MHz in Right Ascension ( $\alpha$ ) and Declination ( $\delta$ ) coordinates visible during *off-zenith* (top) and *zenith* (bottom) pointings. The color scale on the right is logarithmic and is common to both panels. Contours of power pattern shown in figure 4 are overlaid. The contour levels shown are 0.001953125, 0.0078125, 0.03125, 0.125, and 0.5. The Galactic center and a portion of the Galactic plane are prominently visible during the *off-zenith* pointing and the MWA tile power receptivity is significant ( $\gtrsim 0.125$ ) in that direction. In contrast, emission from the Galactic plane in *zenith* pointing is significantly lesser.



### 6.2.2. Compact Foreground Model

We use a combination of NRAO VLA Sky Survey (NVSS; Condon et al. 1998) at 1.4 GHz and Sydney University Molonglo Sky Survey (SUMSS; Bock et al. 1999; Mauch et al. 2003) at 843 MHz due to their matched flux sensitivity and angular resolution, and complimentary survey footprints covering the entire sky. The SUMSS catalog covers the sky with declination  $\delta < -30^\circ$  with a limiting peak brightness of 6–10 mJy/beam and an angular resolution of  $\sim 45''$ . The NVSS covers the sky with  $\delta > -40^\circ$  with a similar angular resolution and a limiting flux density of  $\approx 2.5$  mJy for discrete sources.

From the SUMSS catalog, we select compact sources whose deconvolved major axes are equal to  $0''$ . From the NVSS catalog, we excluded objects that overlap with those in the SUMSS survey footprint. Compact sources from NVSS were selected if the convolved major axes were not greater than  $\approx 47''$ , which is almost equal to the angular resolution of the survey. Using a mean spectral index of  $\langle \alpha_{\text{sp}} \rangle = -0.83$  (flux density,  $S(f) \propto f^{\alpha_{\text{sp}}}$ ) obtained by Mauch et al. (2003) for both NVSS and SUMSS catalog objects, we calculate the corresponding flux densities at 185 MHz,  $S_{185}$ . From this subset, we choose compact objects with  $S_{185} \geq 10$  Jy. The selection of such bright compact objects is not affected by minor differences in sensitivity of the two surveys. We verified that our selection criteria ensure a similar areal density of sources in the two surveys.

Based on these criteria, we selected 133 sources from the SUMSS catalog and 336 sources from the NVSS catalog. Together with the diffuse foreground model, we obtain an all-sky foreground model consisting of both compact and diffuse emission.

### 6.3. Comparison with Data

With the aforementioned all-sky foreground model, and instrumental and observational parameters, we simulate visibilities using equation 1. Figure 7 shows the amplitude of delay spectrum from *off-zenith* and *zenith* pointings. Notice the qualitative agreement of amplitude and structure with those obtained from data shown in figure 3. The Galactic center and the Galactic plane visible in the *off-zenith* pointing make it appear brighter in the *foreground wedge*.

In order to make a quantitative comparison of delay spectra obtained with the MWA data and our simulations, we consider the following uncertainties. Our foreground models are derived from other higher frequency catalogs and sky maps. The inherent spread in spectral index increases the uncertainty while predicting fluxes at the observed frequency. Using simple error propagation, the fractional error in the delay spectrum caused by the spread in spectral index is  $\sim \ln(f_{\text{orig}}/f) \Delta\alpha_{\text{sp}}$ , where,  $f_{\text{orig}}$  is the original frequency at which the catalog or map was created,  $f = 185$  MHz is the observed frequency, and  $\Delta\alpha_{\text{sp}}$  is the spread (HWHM) in spectral index. From Mauch et al. (2003), we assume  $\Delta\alpha_{\text{sp}} \approx 0.35$  for compact sources from NVSS and SUMSS catalogs. Although the model of de Oliveira-Costa et al. (2008) yields a spectral index per direction on the sky, we assume similar uncertainties exist in spectral indices of our diffuse sky model as well, which is predominantly derived from 408 MHz map of Haslam et al. (1982). Thus, fractional errors in

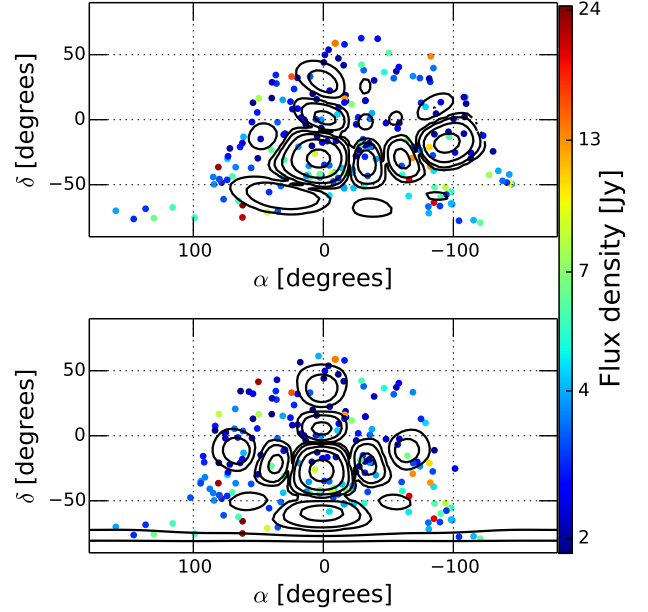


**Figure 6.** Flux densities (in Jy) of bright compact sources at 185 MHz in Right Ascension ( $\alpha$ ) and Declination ( $\delta$ ) coordinates visible during *off-zenith* (top) and *zenith* (bottom) pointings. The color scale on the right is logarithmic and is common to both panels and corresponds to the color-coded filled circles. Contours of power pattern shown in figure 4 are overlaid. The contour levels shown are 0.001953125, 0.0078125, 0.03125, 0.125, and 0.5. The locations of bright compact sources appear to be random.

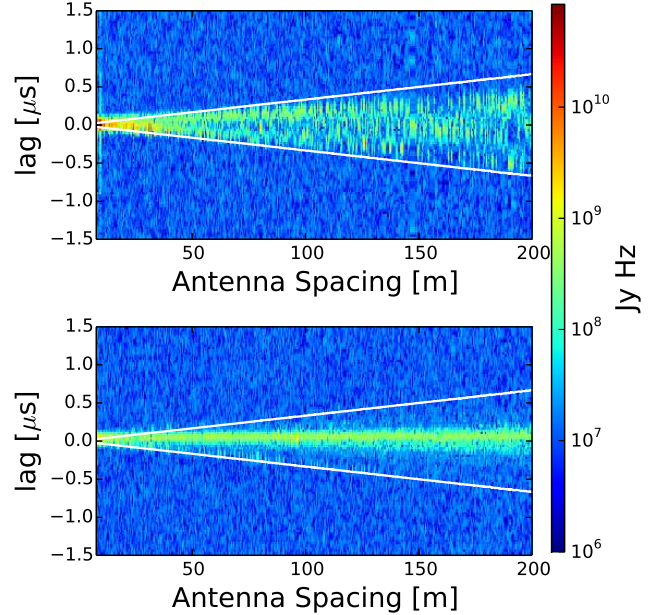


**Figure 7.** Delay spectrum amplitude,  $|V_\eta(|\vec{x}|, \eta)|$  (in units of Jy Hz), obtained with simulations for *off-zenith* (top) and *zenith* (bottom) pointings. White lines mark the boundaries of *foreground wedge* determined by the horizon delay limit and antenna spacing. The features resemble those obtained with MWA data shown in figure 3. The Galactic center and Galactic plane prominently visible in the *off-zenith* pointing makes the emission in the *foreground wedge* brighter relative to that in the *zenith* pointing. The axes and color scale are identical to those in figure 3.

delay spectrum from compact foreground objects and dif-

fuse emission are  $\sim 0.7$  and  $\sim 0.3$  respectively. In addition, delay spectra from simulations and data each have uncertainties due to thermal noise with rms,  $\Delta V_{\eta}^N(|\bar{\mathbf{x}}|, \eta) \sim 1.4 \times 10^7$  Jy Hz, where the superscript N stands for thermal noise. We estimate the ratio of delay spectra from data and simulations as,  $\rho = |V_{\eta}^D(|\bar{\mathbf{x}}|, \eta)| / |V_{\eta}^S(|\bar{\mathbf{x}}|, \eta)|$ , where superscripts D and S denote data and simulation respectively.

Figure 8 shows histograms of distribution of  $\log_{10} \rho$  for the *off-zenith* (top panel) and *zenith* (bottom panel) pointings respectively inside the *foreground wedge*. The median absolute deviation from these distributions correspond to  $\sim 90\%$  fractional difference between data and modeling on average in either case. This is in line with aforementioned uncertainties in foreground models and thermal noise in measurements. Currently we are significantly limited by unavailability of all-sky foreground models at the observed frequency of 185 MHz. Availability of an accurate foreground model will improve the agreement of simulations with observed data.

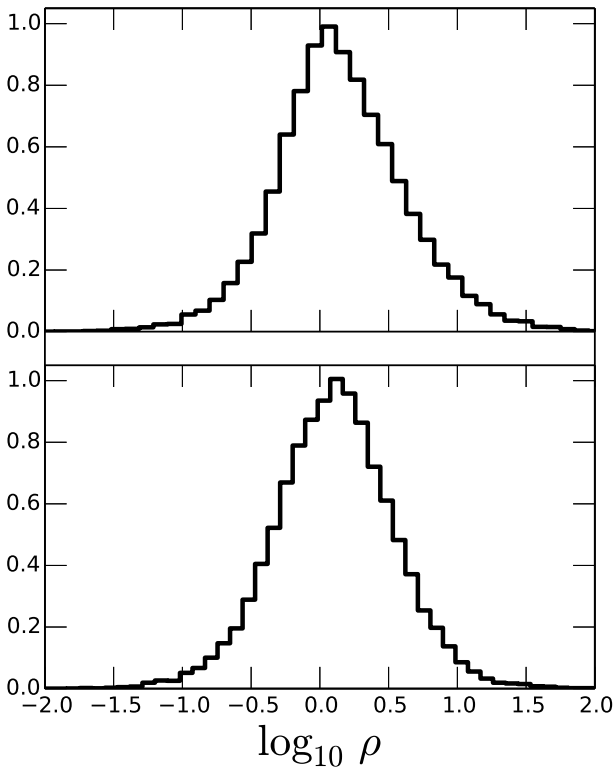


**Figure 8.** Histogram of logarithm of ratio of observed to simulated visibilities restricted to the *foreground wedge* for the *off-zenith* (top) and *zenith* (bottom) pointings. Median absolute deviations of  $\log_{10} \rho$  are 0.29 and 0.27 respectively. A value of zero indicates when the ratio  $\rho = 1$ .

These uncertainties are presented only to confirm the qualitative agreement already seen between figures 3 and 7 and are not intended to serve as a comprehensive estimate of all uncertainties involved. However, since we have not accounted for numerous other uncertainties, especially in the data, such as uncertainties in the antenna power pattern, calibration, radio frequency interference (RFI), and wide field imaging effects, our estimates are conservative. Accounting for such uncertainties will only

improve our confidence level in this comparison. Our primary objective is to explore in detail the foreground signatures embedded in the *foreground wedge*.

## 7. DELAY SPECTRUM ANALYSIS

Having established that results from modeling match those from data, we proceed to examine in further detail the signatures seen in the modeled delay spectra.

A number of factors are responsible for the characteristics noted in the delay spectra obtained from data and through modeling. We address these factors below:

- Sky Model:** Our model of the sky consists of bright compact sources and diffuse emission on diverse spatial scales as seen from figures 5 and 6. It also consists of localized regions of strong emission such as the Galactic plane and Galactic center. The resulting sky emission is anisotropic. In fact, the patch of sky for MWA observations is chosen from regions of low foreground emission. In our detailed study, we have divided the transiting sky into four different “bow-tie” shaped regions with equal areas around zenith as the origin. This results in the ability to attribute the features in the delay spectrum to eight different sectors of the sky.
- Interferometer Orientation:** Since the spatial structure of our foreground model is not expected to be isotropic, we divide our interferometer antenna spacings by their orientation ( $\theta_b$ ) measured counter-clockwise from East. We use the following bins:  $-67.5 \leq \theta_b < -22.5$ ,  $-22.5 \leq \theta_b < 22.5$ ,  $22.5 \leq \theta_b < 67.5$ , and  $67.5 \leq \theta_b < 112.5$ . The bin centers are oriented towards South-East, East, North-East, and North respectively. Since the delays registered at an interferometer depend on the orientation of its antenna spacing vector, binning by interferometer orientation allows us to attribute the delay spectrum to different sky directions.
- Tile Pointing and Power Pattern:** Since the MWA tiles are steered electronically, the power pattern of the tile changes in any observing mode that tracks the source. Our observations consist of a combination of allowing the sky to drift and tracking the sky. In our study, we take into account the effect of changing power pattern of the antennas on the delay spectrum (figure 4). The LST of our data ranges from  $\sim 21$  hours through  $\sim 2$  hours, and for our analysis we chose *off-zenith* and *zenith* pointings shown in figure 2.
- Instrumental Passband:** The instrumental passband characteristics have a direct effect on the delay transform owing to a Fourier relationship between the two. Due to excision of noisy and aliased edge channels repeated in each coarse channel of our passband, we saw repeated patterns of the *foreground wedge* in the delay spectra. As already mentioned earlier, we have used the deconvolution algorithm (*CLEAN*) to rid the delay spectra of band shape effects. Since this paper focuses on studying the effects of foreground on the delay spectra, we do not pursue the characterization of artifacts from the band shape and imperfections in *CLEAN* deconvolution.

The foreground signatures we henceforth identify in the delay spectrum are characterized as arising out of the aforementioned factors. Due to numerous combinations of such factors, we use unique annotations to characterize these signatures.

It may be noted that numerous features overlap at varying levels of significance as a result of various combinations of parameters. We assign the features to their predominant causes. Secondly, we have used noiseless cases to clearly illustrate the observed foreground signatures. With the addition of noise in the visibilities which is subject to observing time, some of the weaker features may not be as prominently visible. Since the foreground signatures are far too numerous and they reside in a vast volume of parameter space such as interferometer orientation, power pattern, patch of sky under observation, and instrumental configuration, we highlight only some examples of the most notable features observed in the delay spectrum of foreground emission.

### 7.1. Diffuse Foregrounds

Figure 9 shows the amplitude of delay spectrum,  $|V_\eta(\bar{\mathbf{x}}, \eta)|$ , simulated with the diffuse foreground model. The top and bottom panels correspond to *off-zenith* and *zenith* pointings respectively.

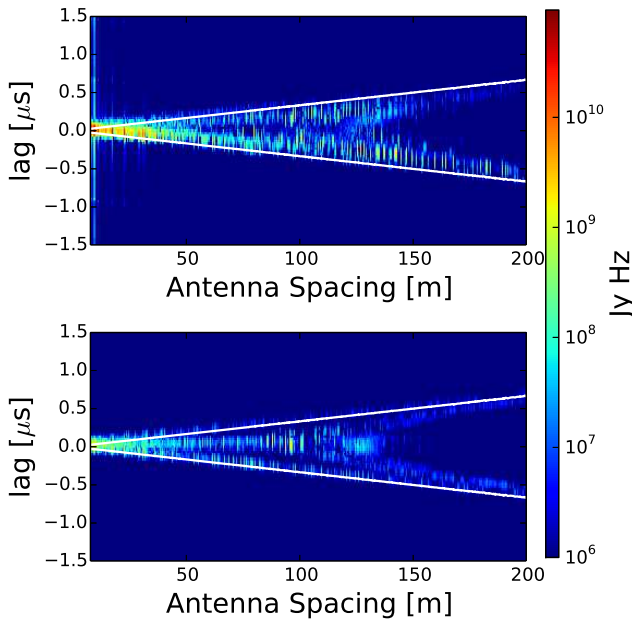


**Figure 9.** Delay spectrum amplitude,  $|V_\eta(\bar{\mathbf{x}}, \eta)|$  (in units of Jy Hz), obtained with simulations for *off-zenith* (top) and *zenith* (bottom) pointings for the diffuse foreground model without any thermal noise. White lines mark the boundaries of *foreground wedge* determined by the horizon delay limit and antenna spacing. The logarithmic color scale is common to both panels. In the *zenith* pointing, diffuse emission delay spectrum has a *two-pronged fork*-shaped structure and is present even at wide antenna spacings.

Here we examine in detail some examples of interesting features observed with the diffuse foreground model.

#### 7.1.1. Galactic Center on Eastward Antenna Spacings

The most prominent signature seen in the *off-zenith* pointing (top panel of figure 9) is due to the bright Galac-

tic center situated on the far west on one of the sidelobes of the power pattern. It appears as a bright branch in the delay spectrum near the negative delay horizon delay limit. This feature is strongest at short antenna spacings and fades with increase in antenna spacing. This Galactic center signature is almost invisible in the *zenith* pointing because the Galactic center has already set over the horizon (see bottom panel in figure 9).

#### 7.1.2. Diffuse Emission

Diffuse emission from the main lobe of the power patterns manifests as a branch at the top with positive delays and a zero-delay horizontal branch in the *off-zenith* and *zenith* pointings respectively, seen in figure 9. The former is seen at positive delays because the main lobe of the power pattern is centered eastward of zenith, whereas in the latter it is centered at zenith. The horizontal arm in the *zenith* pointing fades away on antenna spacings wider than  $\gtrsim 125$  m indicating that the diffuse emission is devoid of spatial structures on scales  $\lesssim 0^\circ 75$ .

#### 7.1.3. Diffuse Emission on Wide Antenna Spacings

A very interesting signature of diffuse emission is revealed at regions near the positive horizon delay limit in the *off-zenith* pointing and at both positive and negative horizon delay limits in the *zenith* pointing even on wide antenna spacings ( $125 \text{ m} \lesssim \bar{x} \leq 200 \text{ m}$ ) contrary to expectations, which are not expected to be sensitive to diffuse emission. We claim this is because wide antenna spacings appear shortened due to projection effects when sensitivity towards off-axis emission, especially towards the horizon, is concerned. It naturally holds for short antenna spacings as well. Thus, diffuse emission from far off-axis directions manifests as an edge-heavy *two-pronged fork* across all antenna spacings. It decreases in strength with increasing antenna spacing as expected but is present in all orientations of the antenna spacing vector. This contributes to a *pitchfork*-shaped feature which will be discussed later in §7.3.1 in more detail.

### 7.2. Compact Foregrounds

Figure 10 shows the delay spectrum arising out of our compact objects sky model for *off-zenith* and *zenith* pointings (shown in figure 6) in the top and bottom panels respectively.

In contrast to delay spectrum of diffuse emission, compact emission manifests as a center-heavy structure in the delay spectrum with either pointing. This contributes to the *pitchfork* feature which will be discussed in detail in §7.3.1. Below we summarize some specific notable features obtained with our compact objects foreground model.

#### 7.2.1. Compact Emission in Power Pattern Main Lobe

Since the main lobe of the power pattern in the *off-zenith* pointing is centered eastward of zenith, bulk of the compact foreground emission is seen in a branch with positive delay but short of the positive horizon delay limit. Compact emission from the same patch of sky is seen as a bright horizontal arm at zero delay in the *zenith* pointing since the main lobe of the power pattern is centered at zenith.



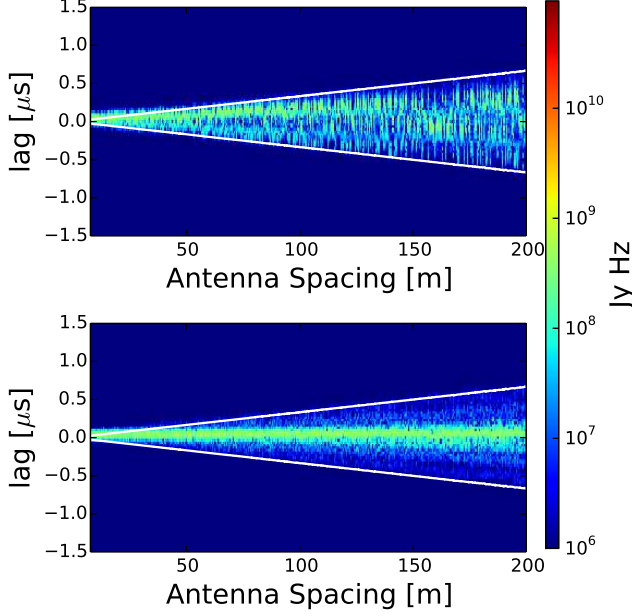


**Figure 10.** Delay spectrum amplitude,  $|V_\eta(\bar{x}, \eta)|$  (in units of Jy Hz), obtained with simulations for *off-zenith* (top) and *zenith* (bottom) pointings for the compact objects foreground model without any thermal noise. White lines mark the boundaries of *foreground wedge* determined by the horizon delay limit and antenna spacing. The logarithmic color scale is identical to that in figure 9. Emission from compact objects gives rise to centrally concentrated features in the *foreground wedge*.

### 7.2.2. Compact Emission in Power Pattern Sidelobes

Foreground emission in zero delay and negative delay regions in the *off-zenith* pointing is caused by compact objects co-located with sidelobes of the power pattern. On the other hand, compact objects co-located with sidelobes of power pattern in the *zenith* pointing are revealed as distinct but faint branches at positive and negative delays depending on the orientation of antenna spacing and direction of emission on the sky.

### 7.3. All-Sky Composite Foreground Model

Delay spectra from the all-sky foreground model in our study display a composite feature set drawn from the features of compact and diffuse foreground models. Here we compare the relative strengths of emission from different spatial scales in our all-sky composite foreground model.

#### 7.3.1. Pitchfork Effect

Excluding the bright emission from the Galactic center which is heavily dependent on the sky location pointed to by the antenna, delay spectrum resulting from the all-sky composite foreground model consists of signatures already noted in the diffuse and compact foreground cases. This is illustrated by a microscopic examination of the *zenith* pointing in our study.

Figure 11 shows delay spectra of three interferometers of different antenna spacings oriented northward during the *zenith* pointing. The diffuse, compact, and composite components are shown as dotted, dashed, and solid lines respectively. The horizon delay limits are shown as vertical dot-dashed lines. The gray shaded area denotes the envelope of expected uncertainty in the delay spectrum. This uncertainty is dominated by the spread in

spectral index of compact foreground objects inside the *foreground wedge* (between the horizon delay limits) proportional to the delay spectrum from compact objects, and by thermal noise outside the horizon delay limits.

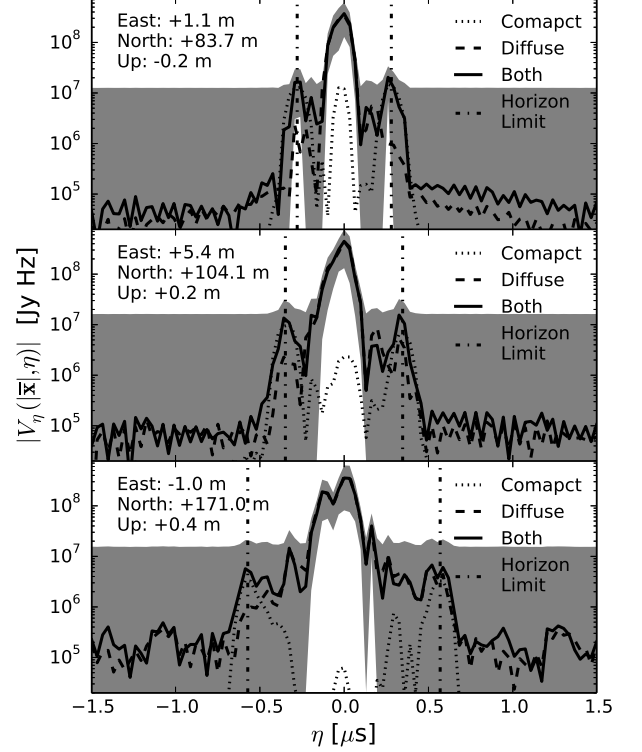


**Figure 11.** Absolute value of delay spectrum,  $|V_\eta(\bar{x}, \eta)|$ , for three chosen antenna spacings,  $\sim 84$  m (top),  $\sim 105$  m (middle), and  $\sim 170$  m (bottom). The antenna spacing vector is specified in each panel along East, North and Upward directions. The dotted, dashed and solid lines denote contributions from diffuse emission, compact objects and composite foreground model respectively. The dot-dashed lines mark the horizon delay limits. The shaded region denotes the envelope of uncertainty around expected values for composite model. This uncertainty is dictated by uncertainties in spectral indices of foreground models inside the delay horizon delay limits. Outside the horizon delay limits, it is predominantly due to thermal noise. Compact objects dominate the central regions of power spectrum while both components, especially diffuse emission on short antenna spacings, dominate near the horizon delay limits, giving rise to a *pitchfork*-shaped structure.

The zero-delay peak (corresponding to the main lobe in the power pattern) with a value of  $\sim 10^8$ – $10^9$  Jy Hz, independent of antenna spacing, is predominantly determined by compact foreground objects. The corresponding peak at zero-delay from diffuse foreground model is at least 10 times fainter and decreases drastically with increase in antenna spacing. This is the response expected from different antenna spacings towards compact and diffuse foreground objects.

Near the horizon delay limits at shorter antenna spacing, diffuse emission is brighter than that from compact objects. With increasing antenna spacing, although diffuse and compact components of emission become comparable, diffuse emission does not decrease as rapidly as

seen at zero-delay. In fact, even with widely spaced antennas, diffuse emission in the delay spectrum near the horizon delay limits exceeds that in the main lobe by more than two orders of magnitude. This is due to apparent shortening of antenna spacing owing to projection effects while receiving emission from wide off-axis directions. This demonstrates the edge-heavy *two-pronged fork* feature discussed in §7.1.3.

The resulting delay spectrum from a composite foreground model that combines diffuse and compact object emission consists of center-heavy features on all antenna spacings from compact objects and edge-heavy features from both components especially diffuse emission even on wide antenna spacings. Henceforth, we call this as the *pitchfork* structure in the *foreground wedge*.

All these observations are consistent with those from figures 9 and 10. The observability of the predicted *pitchfork* signature depends on the relative levels of uncertainty in the foreground model and thermal noise. In our simulations, since thermal noise is  $\gtrsim 10^7$  Jy Hz, and features near the horizon delay limits are  $\sim 10^7$  Jy Hz, the *pitchfork* feature is not expected to be detected in a noisy scenario although this feature is marginally visible in the *zenith* pointing of the observed data (see figure 3). We attribute this to differences between our foreground model and the actual sky. However, with improvements to the foreground model and instrument configuration that can reduce thermal noise and other systematic uncertainties, we are confident the *pitchfork* signature in delay spectrum will be observed with high significance.

We also note that increasing the antenna spacing results in progressively improving the resolution along delay axis by increasing the number of delay bins inside the *foreground wedge*. This improves the localization of foreground objects whose signatures are imprinted in the delay spectrum. For instance, there is an increase in the number of secondary peaks in the delay spectrum between zero-delay and horizon delay limits as antenna spacing increases from  $\sim 84$  m to  $\sim 170$  m. In this case, these correspond to sidelobes of the power pattern that lie between the main lobe and the horizon along the North-South direction. In interferometers with short spacings, due to relatively lower resolution along delay axis inside the *foreground wedge* and a consequent loss of localization of direction of foreground emission, these secondary peaks blend in with other major peaks and are not distinctly visible. These findings are consistent with discussion in §7.2.2.

In summary, the brightest signature ( $\gtrsim 10^{10}$  Jy Hz) is that of the Galactic center in the *off-zenith* pointing co-located at a westward sidelobe with a significantly high gain. The next brightest signature ( $\sim 10^8 \sim 10^9$  Jy Hz) is caused by compact emission appearing to be concentrated in the inner regions of the foreground wedge (near zero delays) rather than towards the edges. Diffuse emission co-located at the main lobe of the power pattern is fainter by approximately an order of magnitude relative to compact emission from the same region for a  $\sim 84$  m antenna spacing but unlike the latter, diffuse emission decreases rapidly by over two orders of magnitude as antenna spacing is widened to  $\sim 170$  m. However, diffuse emission is significantly high near horizon delay limits compared to main lobe of the power pattern as antenna spacing is widened. This leads to edge-heavy features in

the delay spectrum. Complemented by the center-heavy compact foreground features, we have demonstrated the presence of a *three-pronged pitchfork*-shaped signature in the delay spectrum of foreground sky.

## 8. SCREENING OF SEVERE FOREGROUND CONTAMINATED INTERFEROMETERS

The delay spectrum,  $V_\eta(\bar{\mathbf{x}}, \eta)$ , not only carries information on spatial scales of foreground emission but also offers a unique advantage of viewing the sky through a combination of antenna spacing vector and the delay axis. This allows us to programmatically screen data for antenna spacings that are severely contaminated by foregrounds which can be weighted appropriately during data analysis. While the *foreground wedge* is a region of high foreground contamination, of particular interest to the EoR community is foreground contamination near horizon delay limits. These regions are responsible for significant spillover into the relatively clean *EoR window* due to spectral response of the instrument and foregrounds.

With a foreground model known *a priori* in which locations of very bright foreground objects such as the Galactic center or AGN are available, we can predict their response across antenna spacings as a function of observing parameters such as LST, power pattern, etc. Specifically, we can pick interferometers where these bright foreground objects will be visible at delays near horizon delay limits. One such example is already provided in our study. The Galactic center is the most dominant source of foreground contamination in the *off-zenith* pointing. Since it is located in the western sky, it is most distinctly seen near the negative horizon delay limit on eastward oriented antenna spacings in the delay spectrum (see figures 3, 7 and 9, and §7.1.1). In fact these figures illustrate that deconvolution along delay axis is severely hampered by this extreme contamination, thereby leading to leakage beyond the *foreground wedge* into the *EoR window*. In practice, we could downweight these antenna spacings for the specific LST to mitigate the effects of spillover from such foreground contamination in EoR studies. With spatial scales of such objects known, besides downweighting based on antenna spacing orientation, we could also downweight based on antenna spacing distance. For instance, a bright compact object will excite interferometers uniformly across antenna spacings whereas an extended object will gradually fade with increase in antenna spacing.

This provides us with a very simple and yet effective tool in adding a layer of sophistication to mitigate effects of foreground contamination in EoR data analysis.

## 9. SUMMARY

Our primary motivation in this work is to analyze the signatures of foreground components in the measured delay spectrum. Such an analysis will be helpful in extending our knowledge on the challenge posed by foregrounds in studying the EoR and in devising techniques to mitigate contamination of EoR H<sub>I</sub> signal by foreground objects emitting in radio wavelengths. This is one of the first studies that uses an all-sky foreground model to study the resultant signatures on EoR delay spectrum.

Using parameters that match the instrument and EoR observations using the MWA, and an all-sky foreground

model that consists of diffuse emission from a “global sky model” and bright compact sources from the NVSS and SUMSS catalogs, we model delay spectra obtained with the MWA on antenna spacings of length  $\leq 200$  m. We confirm that the modeled delay spectra is in agreement with data obtained with the MWA, to the extent allowed by levels of uncertainty known in the foreground models and thermal noise in measurements.

We use our simulations in a noiseless scenario to identify numerous signatures of different components of foreground emission seen in the delay spectra. We establish the relationship between these signatures and observing parameters such as antenna pointing and LST, instrument parameters such as antenna power pattern and bandpass shape, and foreground parameters such as the nature of emission, spectral index, etc.

The bright Galactic center at the edge of the western horizon co-located with one of the far sidelobes of MWA tile power pattern is the brightest source of foreground contamination in the *off-zenith* pointing. It manifests itself near negative horizon delay limit in the delay spectrum on antenna spacings oriented eastward.

On expected lines, diffuse emission in the primary beam of the antenna power pattern is prominent on shorter antenna spacings  $\lesssim 125$  m corresponding to angular scales  $\gtrsim 0.75^\circ$ . However, the most interesting result is its footprint on wide antenna spacings near the horizon delay limits. This results in a edge-heavy *two-pronged fork*-shaped signature. This is due to apparent shortening of wide antenna spacings in the direction of foreground emission far off-axis thereby retaining their response to extended emission. On the other hand, compact foreground objects predominantly map onto central regions of the *foreground wedge*. Features arising from compact sources coincident with primary beam and sidelobes of antenna power pattern have been noted. In general, compact objects produce delay spectrum signatures that are center-heavy, in clear contrast to those from diffuse emission. A composite all-sky foreground model consisting of diffuse and compact foregrounds combines the characteristic individual shapes into a *pitchfork*-

shaped structure in the *foreground wedge*. This will be distinctly visible when the thermal noise floor is sufficiently lowered.

We also provide a simple and effective tool based on the delay spectrum technique to mitigate foreground contamination in EoR data analysis. It is possible to screen interferometers most affected by foreground contamination as a function of antenna spacing vector and time of observation, which can then be assigned optimal weights in the EoR data analysis chain.

This scientific work makes use of the Murchison Radio-astronomy Observatory, operated by CSIRO. We acknowledge the Wajarri Yamatji people as the traditional owners of the Observatory site. Support for the MWA comes from the U.S. National Science Foundation (grants AST-0457585, PHY-0835713, CAREER-0847753, and AST-0908884), the Australian Research Council (LIEF grants LE0775621 and LE0882938), the U.S. Air Force Office of Scientific Research (grant FA9550-0510247), and the Centre for All-sky Astrophysics (an Australian Research Council Centre of Excellence funded by grant CE110001020). Support is also provided by the Smithsonian Astrophysical Observatory, the MIT School of Science, the Raman Research Institute, the Australian National University, and the Victoria University of Wellington (via grant MED-E1799 from the New Zealand Ministry of Economic Development and an IBM Shared University Research Grant). The Australian Federal government provides additional support via the Commonwealth Scientific and Industrial Research Organisation (CSIRO), National Collaborative Research Infrastructure Strategy, Education Investment Fund, and the Australia India Strategic Research Fund, and Astronomy Australia Limited, under contract to Curtin University. We acknowledge the iVEC Petabyte Data Store, the Initiative in Innovative Computing and the CUDA Center for Excellence sponsored by NVIDIA at Harvard University, and the International Centre for Radio Astronomy Research (ICRAR), a Joint Venture of Curtin University and The University of Western Australia, funded by the Western Australian State government.

## APPENDIX

### REFERENCES

- Beardsley, A. P., Hazelton, B. J., Morales, M. F., et al. 2012, MNRAS, 425, 1781  
 —. 2013, MNRAS, 429, L5  
 Bock, D. C.-J., Large, M. I., & Sadler, E. M. 1999, AJ, 117, 1578  
 Bowman, J. D., Morales, M. F., & Hewitt, J. N. 2009, ApJ, 695, 183  
 Condon, J. J., Cotton, W. D., Greisen, E. W., et al. 1998, AJ, 115, 1693  
 Datta, A., Bowman, J. D., & Carilli, C. L. 2010, ApJ, 724, 526  
 de Oliveira-Costa, A., Tegmark, M., Gaensler, B. M., et al. 2008, MNRAS, 388, 247  
 Di Matteo, T., Perna, R., Abel, T., & Rees, M. J. 2002, ApJ, 564, 576  
 Dillon, J. S., Liu, A., & Tegmark, M. 2013, Phys. Rev. D, 87, 043005  
 Furlanetto, S. R., Oh, S. P., & Briggs, F. H. 2006, Phys. Rep., 433, 181  
 Haslam, C. G. T., Salter, C. J., Stoffel, H., & Wilson, W. E. 1982, A&AS, 47, 1  
 Liu, A., & Tegmark, M. 2011, Phys. Rev. D, 83, 103006  
 Lonsdale, C. J., Cappallo, R. J., Morales, M. F., et al. 2009, IEEE Proceedings, 97, 1497  
 Mauch, T., Murphy, T., Buttery, H. J., et al. 2003, MNRAS, 342, 1117  
 Morales, M. F., Bowman, J. D., & Hewitt, J. N. 2006, ApJ, 648, 767  
 Morales, M. F., Hazelton, B., Sullivan, I., & Beardsley, A. 2012, ApJ, 752, 137  
 Morales, M. F., & Hewitt, J. 2004, ApJ, 615, 7  
 Parsons, A. R., & Backer, D. C. 2009, AJ, 138, 219  
 Parsons, A. R., Pober, J. C., Aguirre, J. E., et al. 2012, ApJ, 756, 165  
 Parsons, A. R., Backer, D. C., Foster, G. S., et al. 2010, AJ, 139, 1468  
 Pober, J. C., Parsons, A. R., Aguirre, J. E., et al. 2013, ApJ, 768, L36  
 Taylor, G. B., Carilli, C. L., & Perley, R. A., eds. 1999, Astronomical Society of the Pacific Conference Series, Vol. 180, Synthesis Imaging in Radio Astronomy II  
 Thyagarajan, N., Udaya Shankar, N., Subrahmanyan, R., et al. 2013, ApJ, 776, 6

- Tingay, S. J., Goeke, R., Bowman, J. D., et al. 2013, *PASA*, 30, 7
- Trott, C. M., Wayth, R. B., & Tingay, S. J. 2012, *ApJ*, 757, 101
- van Haarlem, M. P., Wise, M. W., Gunst, A. W., et al. 2013, *A&A*, 556, A2
- Vedantham, H., Udaya Shankar, N., & Subrahmanyam, R. 2012, *ApJ*, 745, 176
- Zaldarriaga, M., Furlanetto, S. R., & Hernquist, L. 2004, *ApJ*, 608, 622